Geophysical Research Letters

RESEARCH LETTER
10.1029/2023GL104357

Key Points:

- Horizontal wavenumber spectra across the middle atmosphere are computed using airborne lidar observations during the 2019 sudden stratospheric warming (SSW)
- Horizontal wavenumber spectra are close to $k^{-5/3}$ in the stratosphere, and become shallower in the mesosphere during the SSW
- Observational evidence is provided that the mesoscale spectral slope in the middle atmosphere is caused by the occurrence of gravity waves

Supporting Information:

Supporting Information may be found in the online version of this article.

Correspondence to:
S. Knobloch,
stefanie.knobloch@dlr.de

Citation:
Knobloch, S., Kaifler, B., Dörnbrack, A., & Rapp, M. (2023). Horizontal wavenumber spectra across the middle atmosphere from airborne lidar observations during the 2019 southern hemispheric SSW. *Geophysical Research Letters*, *50*, e2023GL104357. https://doi.org/10.1029/2023GL104357

Received 2 MAY 2023
Accepted 8 JUL 2023

Horizontal Wavenumber Spectra Across the Middle Atmosphere From Airborne Lidar Observations During the 2019 Southern Hemispheric SSW

Stefanie Knobloch[1], Bernd Kaifler[1], Andreas Dörnbrack[1], and Markus Rapp[1,2]

[1]Institut für Physik der Atmosphäre, Deutsches Zentrum für Luft- und Raumfahrt, Oberpfaffenhofen, Germany, [2]Meteorologisches Institut München, Ludwig-Maximilians-Universität München, Munich, Germany

Abstract Horizontal wavenumber spectra across the middle atmosphere are investigated based on density measurements with the Airborne Lidar for Middle Atmosphere research (ALIMA) in the vicinity of the Southern Andes, the Drake passage and the Antarctic peninsula in September 2019. The probed horizontal scales range from 2000 to 25 km. Spectral slopes are close to $k^{-5/3}$ in the stratosphere and get shallower for horizontal wavelengths <200 km in the mesosphere. The spectral slopes are shown to be statistically robust with the presented number of flight legs despite the unknown orientation of true wave vectors relative to the flight track using synthetic data and a Monte Carlo approach. The largest spectral amplitudes are found over the ocean rather than over topography. The 2019 sudden stratospheric warming caused a critical level for MWs and a reduction of spectral amplitudes at horizontal wavelengths of about 200 km in the mesosphere.

Plain Language Summary The spectral analysis of observations along extended flight tracks helps to determine the contribution of different length scales to atmospheric processes. In this study we calculate horizontal wavenumber spectra in the altitude range between 20 and 80 km, the middle atmosphere, based on observations from the Airborne Lidar for Middle Atmosphere research onboard the HALO aircraft. The observations were performed in the vicinity of the Southern Andes, the Drake passage and the Antarctic peninsula during September 2019. The observed horizontal scales range from 2000 km to about 25 km and cover almost the entire mesoscale range of atmospheric dynamics in the middle atmosphere. This study finds that vertical oscillations in the atmosphere, called gravity waves, cause the slopes and power of the spectra at the observed horizontal scales in the middle atmosphere. The slopes and power of the horizontal spectra vary with varying gravity wave activity during the period of observations.

1. Introduction

The first research flights with an upward-pointing airborne lidar were conducted by Kwon et al. (1990) and Hostetler et al. (1991) who computed horizontal and vertical wavenumber spectra between 80 and 100 km altitude from measurements acquired with an airborne Na lidar. Hostetler and Gardner (1994) combined Rayleigh and Na lidar observations to cover altitudes from 25 to 40 km and 80–105 km while Rayleigh lidar observations from Gao and Meriwether (1998) ranged from 30 to 45 km. All the findings from these early airborne lidar studies have in common that their horizontal wavenumber spectra in the troposphere, stratosphere and upper mesosphere support gravity waves (GW) as the underlying dynamical process for determining the horizontal wavenumber dependence in the mesoscale range.

The mesoscale dynamics are characterized by horizontally rotational and horizontally divergent modes. In theoretical work it has been argued that the horizontal wavenumber dependence can be described by stratified turbulence associated with a forward inertial energy cascade (Brune & Becker, 2013; Li & Lindborg, 2018; Lindborg, 2006) or by GWs associated with an inertial energy cascade from larger to smaller scales (Bacmeister et al., 1996; Dewan, 1979; Gao & Meriwether, 1998; Hostetler & Gardner, 1994; VanZandt, 1982), including further work on saturated-cascade (Dewan, 1994, 1997), linear-instability (Gardner et al., 1993) and diffusive filtering of GWs (Gardner, 1994).

Recent studies using idealized and numerical weather prediction (NWP) simulations indicate that the mesoscale $k^{-5/3}$ spectral shape, with k as horizontal wavenumber, is influenced by buoyancy driven motions and by an inertial energy cascade (Menchaca & Durran, 2019; Selz et al., 2019; Sun et al., 2017; Waite & Snyder, 2009).

Menchaca and Durran (2019) found that MWs have a major impact on the energy spectrum: linear waves entirely constitute the divergent mode while breaking waves energize rotational and divergent modes.

The questions which dynamical mechanism underlies the mesoscale $k^{-5/3}$ spectrum and whether there is a universal dynamical mechanism at all have still not been unequivocally answered, as studies suggest that the spectral energy is rather intermittent because of the intermittency of the dynamical processes, for example, convection or GWs (Menchaca & Durran, 2019; Selz et al., 2019). However, knowing and understanding the atmospheric spectra is of importance for NWP and atmospheric predictability (Charney, 1971), and for the development and application of GW parameterizations in all layers of the atmosphere (Harvey et al., 2022; Kim et al., 2003; Plougonven et al., 2020).

In this paper we close the gap in altitude coverage of previous measurements and present horizontal wavenumber spectra of lidar photon counts (proportional to density) across the middle atmosphere from 20 to 80 km altitude. The spectra were calculated from measurements by Airborne Lidar for Middle Atmosphere research (ALIMA) onboard the High Altitude and Long Range Research Aircraft (HALO) taken during the Southern Hemisphere Transport, Dynamics, and Chemistry – Gravity Waves (SouthTRAC–GW) campaign in 2019 (Rapp et al., 2021). The campaign covered the period of the 2019 Southern Hemisphere (SH) sudden stratospheric warming (SSW) (e.g., Lim et al., 2021; Shen et al., 2020). The aim of the study is to investigate the horizontal wavenumber spectra over the southern hemispheric hotspot for MWs in the middle atmosphere with ALIMA. Recent technological advances since the first airborne lidar observations in the 1990s have improved the data quality, resolution and altitude range of airborne lidar measurements (Kaifler & Kaifler, 2021). Based on these data, we will consider the following research questions:

1. What is the shape of horizontal wavenumber spectra throughout the middle atmosphere in the vicinity of the MW hotspot above the Southern Andes?
2. How are the horizontal wavenumber spectra in the middle atmosphere affected by GWs and the SSW?

The paper is structured as follows: in Section 2 the SouthTRAC–GW campaign, the ALIMA lidar and the spectral analysis are described. In Section 3, we present the middle atmospheric horizontal wavenumber spectra. The consequence of the unknown orientation of wave vectors, the role of GWs and the SSW for the horizontal wavenumber spectra, are discussed in Section 4, followed by our conclusions in Section 5.

2. Description of Measurements and Analysis

2.1. SouthTRAC–GW

SouthTRAC–GW was conducted in the southern part of South America and above the Antarctic peninsula in September 2019 to gather a unique data set comprising temperature and trace gas observations from the troposphere up to the mesosphere (Rapp et al., 2021). The intention was to study MWs near their orographic sources, their vertical and horizontal propagation, and their breaking and dissipation. SouthTRAC–GW delivered measurements for the comparison and validation of other measurement techniques, high-resolutions simulations, and NWP models. The data set used in this study includes measurements from six dedicated MW research flights: ST08 on 11/12, ST09 on 13/14, ST10 on 16/17, ST11 on 18/19, ST12 on 20/21, and ST14 on 25/26 September 2019 (see Table 3 in Rapp et al. (2021)) of HALO. Typical traveled distances are around 7,000 km, within the region from 35°S to 65°S and from 82°W to 46°W, typical crusing altitudes between 10 and 14 km, and typical aircraft ground speeds between 200 ms^{-1} to 300 ms^{-1}.

The campaign period coincided with a rare SH SSW (e.g., Dörnbrack et al., 2020; Lim et al., 2021). The SSW started at the end of August, therefore, all flights were conducted during the SSW.

The tropospheric flow was dominated by blocking ridges upstream of the Southern Andes causing a synoptic flow rather parallel to the mountain ridge in the first week of September 2019 (see Figure 4 in Rapp et al. (2021)). From 8 September 2019 a mostly zonal flow or propagating troughs dominated the tropospheric flow. Because the flights were planned to be temporally aligned with a zonal upstream flow in the troposphere (Bauer et al., 2022), all flight days have in common that there were good excitation conditions of GWs at the Southern Andes and/or Antarctic Peninsula.

Figure S1 in Supporting Information S1 summarizes the six individual flight tracks and the prevailing horizontal winds at 10 hPa. At 10 hPa, the polar night jet (PNJ) was shifted toward the tip of South America with mostly zonal flow during ST08 and ST09. A deformation of the stratospheric polar vortex (more elliptic) induced a strong curvature with strong meridional flow of the PNJ over the Southern Andes at 10 hPa during ST10, ST11, and ST12.

The weakening of the PNJ and the warming of the stratospheric polar vortex caused a critical level for MWs (Rapp et al., 2021). The critical level descended from about 60 km at the beginning of September 2019 to 40 km at the end September 2019 and decreased the MW activity in the upper stratosphere (Kogure et al., 2021; Rapp et al., 2021) and mesosphere (Kohma et al., 2021). The vertical propagation of observed MWs was affected by the SSW during the flights ST09, ST10, ST11, ST12 and ST14, whereas during flight ST08 observed MWs were able to propagate up to 60 km.

2.2. ALIMA

ALIMA is a compact Rayleigh lidar system developed for airborne operation. The instrument consists of an upward pointing frequency-doubled, diode-pumped and pulsed neodymium-doped yttrium aluminum garnet (Nd:YAG) laser with a wavelength of 532 nm, a pulse energy of 125 mJ, and a pulse repetition frequency of 100 Hz; a receiving telescope of 48 cm diameter; a mechanical chopper for gating of backscattered photons from the lowest altitudes to protect the detectors from saturation, and three height-cascaded elastic detector channels (low, mid and far) to cover the full dynamic range of the lidar return signal from the lower stratosphere to the upper mesosphere. The ALIMA photon counts are about two orders of magnitudes larger compared to the first airborne Rayleigh lidar observations by Hostetler and Gardner (1994) and Gao and Meriwether (1998) which highlights the advance of the lidar technology in the last 30 years and allows us to extend our altitude range of observations throughout the entire middle atmosphere.

The photon counts are aggregated in bins of 100 m vertical resolution, are integrated over a period of 10 s and corrected for the dead time of the detectors, the range, the photon background and the attenuation of the laser beam by Rayleigh extinction (a correction for ozone absorption is omitted due to the lack of sufficient ozone observations). The such processed photon counts are proportional to the atmospheric density.

2.3. Spectral Analysis

The horizontal wavenumber spectra presented in this study are based on the range corrected photon counts $\gamma(t, z)$ from ALIMA with t and z denoting time and altitude, respectively. $\gamma(t, z)$ is proportional to atmospheric density and thus horizontal wavenumber spectra are proportional to potential energy. We use the photon counts of the low channel below 30 km, the far channel above 50 km and the mid channel between 30 and 50 km. First, the measurements of each research flight are separated into individual flight legs, which are straight and of near constant pressure altitude. The observations are screened for instrumental effects, for example, temporary drops in the signal-to-noise ratio (SNR) due to misalignment of the laser beam or icing on the laser window. Overall, 43 flight legs with traveled distances between 150 and 2,400 km are considered in the spectral analysis. Detailed information of the individual flight legs can be found in Supporting Information S1. Lidar photon count profiles are temporally integrated to a 1 min resolution and smoothed in the vertical with a 900 m LOWESS (Locally Weighted Scatterplot Smoothing) filter. A filter width of 900 m is large enough to (a) satisfactorily reduce photon noise and (b) small enough to not attenuate vertical scales that are above the noise floor and not noticeably affect the horizontal scales. Second, $\gamma(t, z)$ is normalized by a respective temporal average of each flight leg:

$$\gamma'(t, z) = \frac{\gamma(t, z)}{\overline{\gamma(z)}} \tag{1}$$

The normalization eliminates the exponential decrease of photons counts with altitude due the decreasing air density. Remaining fluctuations of photon counts are either caused by geophysical processes, for example, GWs, or by photon noise.

The spectra are presented as the power spectral density (PSD):

$$PSD_{\gamma} = |\hat{\gamma}'|^2 * \frac{\Delta x^2}{X}, \tag{2}$$

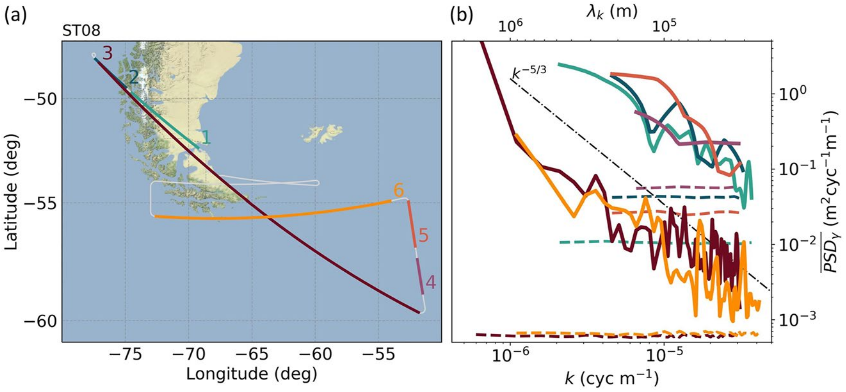

Figure 1. Flight track and individual flight legs of flight ST08 (a) and corresponding mean horizontal wavenumber power spectra of relative density perturbations (b) between 50 and 60 km altitude. Horizontal dashed lines in (b) show the mean horizontal photon noise spectra and the dashed-dotted line indicates a $k^{-5/3}$ slope.

where $\hat{\gamma}'$ is the fast Fourier transform (FFT) of γ'. Δx, and X are the horizontal bin size and the length of a flight leg, respectively. The horizontal wavenumber spectra are calculated between altitudes of 20–80 km for each vertical bin (every 100 m) and, for statistical certainty, averaged over an altitude range of 10 km. Above 80 km the signal is dominated by photon noise.

The horizontal wavenumber k and the horizontal wavelength λ_k are given by:

$$\lambda_k = k \cdot \Delta x, \quad k = [1, 2, 3, \ldots, n], \quad k = \frac{2\pi}{\lambda_k}, \tag{3}$$

where $n = X/\Delta x$ and $\Delta x = \tau \cdot \overline{GS_{HALO}}$ with τ as temporal spacing and $\overline{GS_{HALO}} GS_{HALO}$ as the leg mean ground speed of HALO. During the research flights GS_{HALO} varied due to changing horizontal winds. The actual spacing of the measurements in the horizontal is thus irregular (Cho et al., 1999). However, the absolute error in λ_k due to the usage of a leg mean ground speed instead of the time varying ground speed is small (0.03%–0.9%). The smallest λ_k is typically between 22 and 30 km, considering the sampling rate in space which depends on GS_{HALO}, the temporal integration of 60 s and the Nyquist-frequency.

As the flight legs have different lengths and $\overline{GS_{HALO}}$, the calculated horizontal wavenumber spectra are interpolated to the same values of k and λ_k before averaging over all flight legs and research flights to obtain flight-mean spectra and SouthTRAC–GW-mean spectra.

Additionally, photon noise spectra for each flight leg are calculated based on $\overline{\gamma(z)}$ and the assumption that the photon noise follows a Poisson distribution. The calculation is repeated 1,000 times in a Monte-Carlo experiment. The obtained mean photon noise spectra reveal white noise and are constant over all scales (Figure 1b).

3. Middle Atmospheric Horizontal Wavenumber Spectra

Figure 1 shows an example of the spectral analysis of the individual flight legs between 50 and 60 km altitude from research flight ST08 on the 11 September 2019 23:00 UTC to 12 September 2019 07:00 UTC. Flight legs 1, 2, 4 and 5 are separated because of a temporay drop in the SNR caused by a misalignment of the laser beam. All flight legs of ST08 show a similar slope of $k^{-5/3}$ and are well above their respective noise floors. The largest values of $\overline{PSD_\gamma}$ appear in flight legs 4 and 5 over the Scotia Sea and in flight legs 1 and 2 over Patagonia and the Southern Andes (Figures 1a and 1b).

The distribution of $\overline{PSD_\gamma}$ integrated over the $\lambda_k = 50$ km to $\lambda_k = 150$ km spectral range of all 43 flight legs classified for their position above *Land*, *Ocean* or both (*Land/Ocean*) is shown in Figure 2. The $\overline{PSD_\gamma}$ values were scaled by the respective $\overline{PSD_\gamma}$ of photon noise. This is necessary in order to make flights and legs comparable in $\overline{PSD_\gamma}$. The signal strength strongly varies for the different research flights and decreases with altitude. Hence, the relative impact of the photon noise increases. Therefore, normalized $\overline{PSD_\gamma}$ gets smaller with altitude. The largest values and the greatest variability of $\overline{PSD_\gamma}$ are found above the ocean. However, $\overline{PSD_\gamma}$ is on average

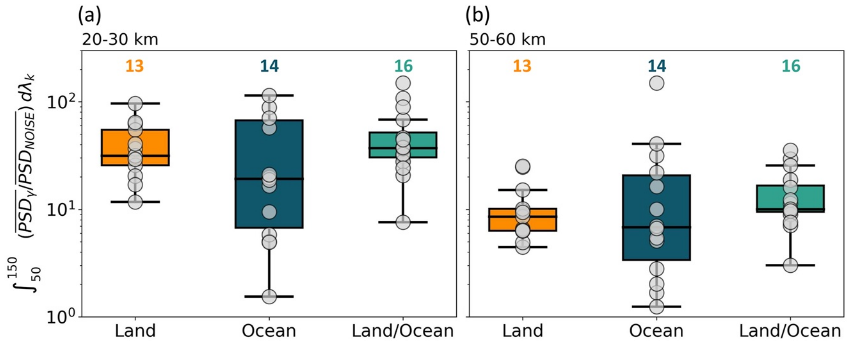

Figure 2. Normailized $\overline{PSD_\gamma}$ integrated over the spectral range $\lambda_k = 50$ km to $\lambda_k = 150$ km of all 43 flight legs in the altitude range 20–30 km (a) and 50–60 km (b) and classified for their position above land, ocean or land/ocean. The boxplots feature the median, 25 and 75 percentiles (inner quartile range), and the whiskers that extend to smallest/largest non-outliers. The colored numbers give the number of legs for each category.

smaller over the ocean than over land. In the stratosphere the 75 percentile and upper whisker of the category above ocean are similar in $\overline{PSD_\gamma}$ to above land (Figure 2a) while in the mesosphere the 75 percentile and upper whisker are larger above the ocean than above land (Figure 2b). Flight legs that were flown above land and ocean include large values of $\overline{PSD_\gamma}$ but a rather small variability of the inner quartile range.

Figure 3 shows the mean horizontal wavenumber spectra of observed photon counts for horizontal scales from 2000 to 22 km between 20 and 80 km altitude. Additionally, the 3σ-value of the photons noise is shown. Normally, the noise floor would be constant across the horizontal wavenumbers (Figure 1b), however due to the averaging of legs of different lengths the variability of the photon noise is the largest for $50 < \lambda_k < 150$ km (all 43 flight legs fall into this range).

Values of normalized $\overline{PSD_\gamma}$ close to 1 indicate the signal approaching the noise floor while values of normalized $\overline{PSD_\gamma}$ larger than the 3σ-value (outside the gray-shaded area) indicate a large SNR and thus statistically significant data. Except for the highest altitude range and research flight ST10, the signal approaches the noise floor, if at all, at the smallest resolved scales. For the highest altitude range from 70 to 80 km the noise limit is reached at $\lambda_k \sim 200$–500 km (Figure 3f). The flight legs of research fight ST10 had a constant but much weaker signal compared to the other flights due to icing of the laser window, which resulted in a higher absolute noise floor.

Generally, the spectral slopes in Figure 3 are close to $k^{-5/3}$ and partly flatten at higher wavenumbers to a shallower spectral slope depending on the altitude range, research flight and the horizontal wavenumber. In the upper stratosphere and mesosphere only the horizontal wavenumber spectra of research flight ST08 (at the beginning of the SSW) follow closely the $k^{-5/3}$ slope while the other research flights (during the SSW) feature a reduction of approximately 25% in $\overline{PSD_\gamma}$ at $\lambda_k \sim 200$ km and a transition to a shallower slope at larger λ_k (Figures 3c–3e).

For all research flights, $\overline{PSD_\gamma}$ increases with altitude. However, due to the normalization applied before averaging, this behavior is not visible anymore in Figure 3. We also want to point out that the signal strength of the lidar return signal affects the $\overline{PSD_\gamma}$ of photon spectra. This becomes apparent at altitudes where switches of detection channels with higher to lower sensitivity take place, for example, smaller $\overline{PSD_\gamma}$ and larger 3σ-values in the altitude ranges 30–40 km and 40–50 km (Figure 3). Finally, few long legs were flown and as a consequence, the averages include ≤ 7 of spectra with $\lambda_k > 1{,}000$ km.

4. Discussion

4.1. Orientation of Wave Vectors

The observed wavelengths are not true wavelengths. The observed wavelength is the distance between wave fronts sampled along the flight track with an unknown angle of intersection. If a wave is sampled at an angle of 60° relative to its wave vector, the true wavelength is half of the observed wavelength. If the angle approaches about 85°, the true wavelength will be about one order of magnitude smaller than the observed wavelength.

The unknown orientation of the observed GWs introduces a complication for the interpretation of the spectral analysis. While sampling multiple waves in one flight leg, we can not necessarily assume that all of them have

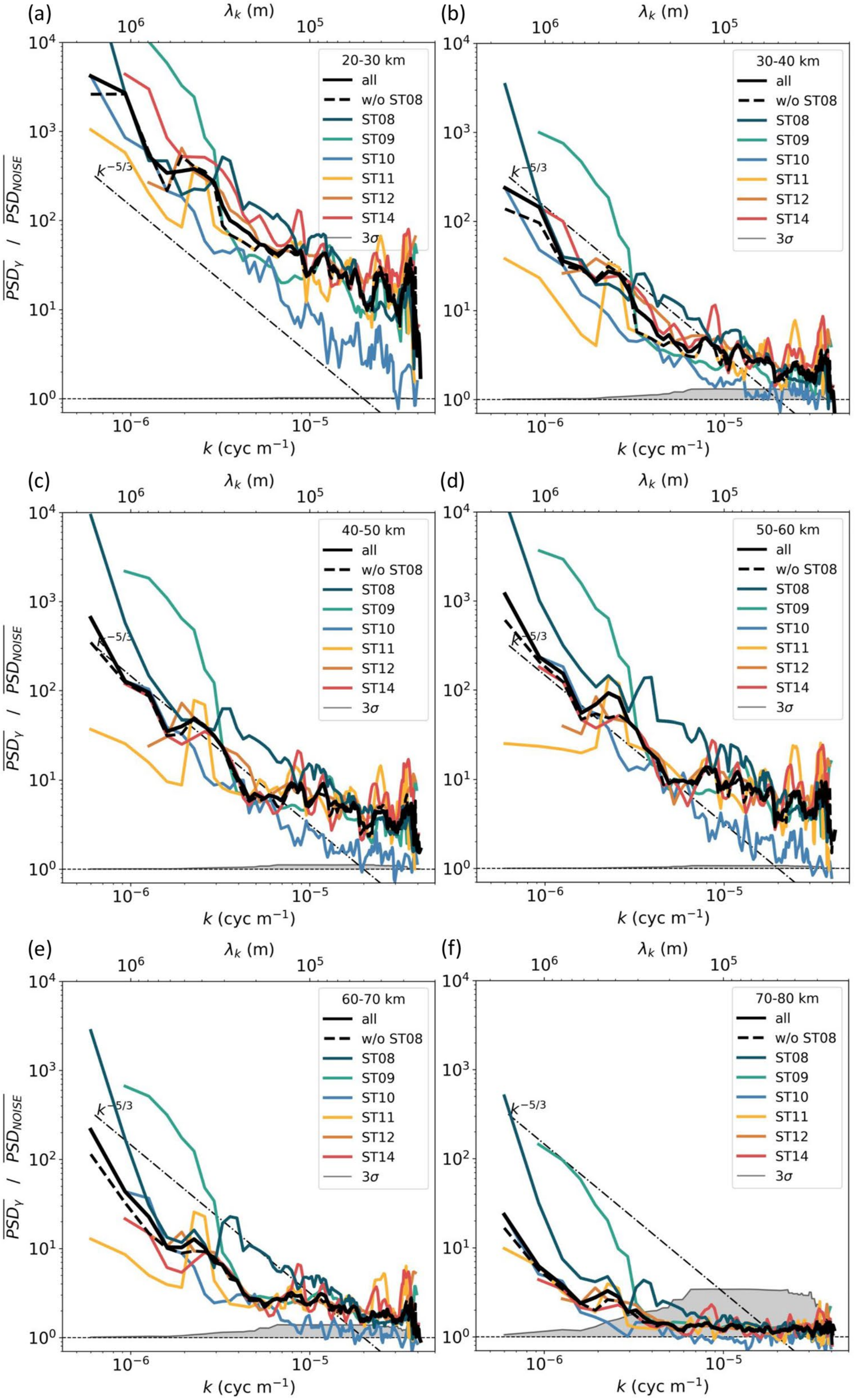

Figure 3. Mean horizontal observed wavenumber spectra of photon counts normalized with the respective photon noise spectra for all research flights (colored lines), the average over all flights (black line) and the average over all flights except ST08 (black dashed line) in the range 20–30 km (a), 30–40 km (b), 40–50 km (c), 50–60 km (d), 60–70 km (e) and 70–80 km (f). The horizontal dashed line marks the noise floor and the gray shading the 3σ-value of photon noise. The dashed-dotted line indicates a $k^{-5/3}$ slope.

the same wave vector. This complication affects all past airborne spectral analyses (e.g., Bacmeister et al., 1996; Cho et al., 1999; Gao & Meriwether, 1998; Hostetler et al., 1991; Hostetler & Gardner, 1994; Kwon et al., 1990; Nastrom & Gage, 1985), and, to our knowledge, has not been discussed previously.

Each observed horizontal wavelength may be shifted to a smaller true horizontal wavelength, which influences the spectral shape. In order to investigate this influence, we performed Monte-Carlo experiments. Each wavenumber of a given horizontal wavenumber spectrum is N times randomly perturbed by a perturbation in wave orientation $0° \leq \alpha \leq 90°$ drawn from a Gaussian (experiment A) with an expected value $\alpha = 0°$ and uniform (experiment B) distribution, for example, $\lambda_k * \cos(\alpha)$. Experiment A represents the case of flight legs which are rather aligned with the wave orientation and experiment B regards a random orientation of flight legs with respect to waves. For both experiments no significant difference (p-value >0.1) but still a large correlation (Pearson coefficient >0.94) were found between the given and the averaged randomly perturbed horizontal wavenumber spectra for $N > 5$ realizations. In general, a shift in horizontal wavenumber can be expected but the experiments reveal only a minor influence on the spectral shape if the number of averaged spectra is sufficiently large ($N > 5$). Therefore, we conclude that the presented flight-means of ST08, ST09, and ST12 and the SouthTRAC–GW-mean spectra are statistically robust in spectral shape for $\lambda_k < 1{,}100$ km. For larger λ_k, the statistics are not statistically robust. The number of legs N of ST10, ST11 and ST14 are <5 (see Table S1). Still, the spectral slopes of these flights are similar to the spectral slopes of ST09, ST14 and the SouthTRAC–GW-mean, suggesting that unknown wave orientations have a negligible impact even in the case of a small number of averaged spectra.

The differences in orientation between the wave vectors and the flight path do not affect the spectral amplitudes as long as at least one full wavelength is sampled. If this condition is not fulfilled, the spectral amplitudes are underestimated.

4.2. Physical Cause of Spectral Slope

The horizontal wavenumber spectra are close to $k^{-5/3}$ in the stratosphere for all observed horizontal scales down to $\lambda_k \approx 100$ km. In the mesosphere, the spectral slope is close to $k^{-5/3}$ for $\lambda_k > 300$ km. For $\lambda_k < 100$ km, the spectral slope tends to be shallower than $k^{-5/3}$, similar to results in the mesopause region found by Kwon et al. (1990). However, why the mesoscale range follows a $k^{-5/3}$ power law dependence (Nastrom & Gage, 1985) or why it deviates from $k^{-5/3}$ (Bacmeister et al., 1996; Hostetler et al., 1991; Kwon et al., 1990), is still an open question for the scientific community.

Lindborg (2006) proposed that GW spectra in the middle atmosphere are affected by stratified turbulence arising from nonlinear dynamics and predicted that observed horizontal GW spectra would exhibit a spectral slope of $k^{-5/3}$. The vertical resolution of the ALIMA observations (100 m grid with 900 m smoothing) is coarser than the vertical resolution needed for the detection of layers of stratified turbulence (Brune & Becker, 2013; Lindborg, 2006). Therefore, and due to the vertical averaging over 10 km altitude ranges, our horizontal wavenumber spectra cannot be associated with stratified turbulence (Rodriguez Imazio et al., 2023) nor can we exclude the occurrence of stratified turbulence. Our findings support the prediction by Lindborg (2006).

4.3. Impact of the SSW

The reduction of $\overline{PSD_\gamma}$ at horizontal wavelengths of about 100–300 km for all research flights except ST08 above 40 km or 50 km altitude was potentially caused by the co-occurring SSW. The SSW induced a critical level for vertically propagating MWs due to the slowing of the PNJ and the displacement of the stratospheric polar vortex. During ST08, the observed MWs were able to propagate up to 65 km altitude while MWs were filtered by the critical level at about 40 km altitude during ST12 (see Figures 4a, 12b, and 12d in Rapp et al. (2021)) and other research flights. The decrease in GW activity in the mesosphere due to the SSW during flights ST09, ST10, ST11, ST12, and ST14 resulted in a decrease of $\overline{PSD_\gamma}$ by 25% in the range 300 km $> \lambda_k >$ 100 km. This result suggests that these are wavelengths of MWs excited by the Southern Andes. Furthermore, the spectra of flights ST09, ST10, ST11, ST12, and ST14 obey no distinct $k^{-5/3}$ slope for 300 km $> \lambda_k >$ 100 km in the mesosphere. This spectral response to the SSW highlights the sensitivity of the horizontal wavenumber spectra to the temporal decline in MW activity and ultimately the absence of MWs. Turning the argument around, the observed decrease in spectral power due to the decreased MW activity during the SSW supports GWs as driver of the $k^{-5/3}$ slope of the mesoscale range in the middle atmosphere.

4.4. Land Versus Ocean

On average, the study found only slightly smaller values of $\overline{PSD_\gamma}$ over ocean than over topography, while the largest individual values occurred over ocean. Previous studies detected an enhanced spectral power above orography compared to smooth terrain or ocean (Gao & Meriwether, 1998; Lilly & Petersen, 1983; Nastrom et al., 1987).

There are two potential causes for the observed enhancement of spectral energy over the ocean: (a) horizontal MW propagation and (b) non-orographic GWs. The large values of $\overline{PSD_\gamma}$ over the ocean were observed during unique stratospheric dynamical conditions associated with the SSW. Generally, the occurrence of a SSW diminishes the MW activity in middle atmosphere and the contribution of non-orographic GWs preponderates. Still, Geldenhuys et al. (2023) and Krasauskas et al. (2023) provided evidence for cases of horizontal MW propagation, for example, refraction, during flight ST08 and ST12.

5. Conclusions

High-resolution and high-quality observations by ALIMA enabled the determination of horizontal wavenumber spectra of density within the horizontal scale range of 2,000 km to about 22 km across the middle atmosphere from 20 to 80 km altitude during SouthTRAC–GW. The presented horizontal wavenumber spectra are the first based on airborne lidar observation between 40 and 80 km altitude and during a SSW.

Our main findings are: (a) the averaged horizontal wavenumber spectra are statistically robust, rather smooth and exhibit slopes close to $k^{-5/3}$ in the stratosphere even though the number of research flights and flight legs was limited; (b) the derived horizontal wavenumber spectra in the middle atmosphere are influenced by horizontally and vertically propagating MWs and potentially non-orographic GWs; and (c) the SSW caused an attenuation of spectral power of the horizontal wavenumber spectra in the mesosphere. The impacts of horizontal MW propagation, non-orographic GWs and GW-SSW interactions on the horizontal wavenumber spectra support the importance to include such processes in future GW parameterizations (Plougonven et al., 2020). However, since SouthTRAC–GW coincided with the SSW, it is difficult to generalize our conclusions, for example, observed deviations from $k^{-5/3}$ for $\lambda_k < 200$ km in the mesosphere might be less distinct or not present during strong stratospheric polar vortex conditions and without a critical level for MWs.

Turning to the research questions we formulated in the beginning, we infer concerning the first question that the derived horizontal wavenumber spectra across the middle atmosphere are close to $k^{-5/3}$. Deviations from this canonical spectral slope mainly appear for $\lambda_k < 300$ km in the mesosphere. Regarding the second question, we conclude MWs and the SSW have a relevant influence on the horizontal wavenumber spectra. Altogether, this study provides observational evidence that the $k^{-5/3}$ spectral slope in the middle atmosphere can be explained by the occurrence of GWs.

Future applications of ALIMA can be used for the studying of horizontal wavenumber spectra of GWs in the middle atmosphere during strong stratospheric polar vortex conditions or the in-depth investigation of horizontal GW propagation. The planned extension of ALIMA by an iron resonance lidar channel (Kaifler et al., 2017) will extend the vertical measurement range into the lower thermosphere and allow for wind measurements. Wind measurements are required for future applications of an airborne lidar in order to estimate the character of the observed GWs.

Acknowledgments
This work was partly funded by the German Federal Ministry for Education and Research under Grant 01 LG 1907A (project WASCLIM) in the frame of the Role of the Middle Atmosphere in Climate (ROMIC)-program. Further support for the SOUTHTRAC mission came from internal funds of the German Aerospace Center, the Karlsruhe Institute of Technology, Forschungszentrum Jülich, and the German Science Foundation (DFG) through the HALO-SPP (DFG-project number 316646266). Further support by DFG under Grant PACOG/RA 1400/6-1 in the frame of the DFG-research group MS–GWAVES is acknowledged. We further thank Erich Becker and one anonymous reviewer for excellent comments that improved the quality of our paper. Open Access funding enabled and organized by Projekt DEAL.

Data Availability Statement

Range-corrected photon count profiles by ALIMA and the output of the spectral analysis may be obtained from https://doi.org/10.5281/zenodo.7861915.

References

Bacmeister, J. T., Eckermann, S. D., Newman, P. A., Lait, L., Chan, K. R., Loewenstein, M., et al. (1996). Stratospheric horizontal wavenumber spectra of winds, potential temperature, and atmospheric tracers observed by high-altitude aircraft. *Journal of Geophysical Research*, *101*(D5), 9441–9470. https://doi.org/10.1029/95JD03835

Bauer, R., Grooß, J.-U., Ungermann, J., Bär, M., Geldenhuys, M., & Hoffmann, L. (2022). The mission support system (MSS v7.0.4) and its use in planning for the SouthTRAC aircraft campaign. *Geoscientific Model Development*, *15*(24), 8983–8997. https://doi.org/10.5194/gmd-15-8983-2022

Brune, S., & Becker, B. (2013). Indications of stratified turbulence in a mechanistic GCM. *Journal of the Atmospheric Sciences*, *70*(1), 231–247. https://doi.org/10.1175/jas-d-12-025.1

Charney, J. G. (1971). Geostrophic turbulence. *Journal of the Atmospheric Sciences*, *28*(6), 1087–1095. https://doi.org/10.1175/1520-0469(1971)028<1087:gt>2.0.co;2

Cho, J. Y. N., Zhu, Y., Newell, R. E., Anderson, B. E., Barrick, J. D., Gregory, G. L., et al. (1999). Horizontal wavenumber spectra of winds, temperature, and trace gases during the Pacific exploratory missions: 1. Climatology. *Journal of Geophysical Research*, *104*(D5), 5697–5716. https://doi.org/10.1029/98JD01825

Dewan, E. M. (1979). Stratospheric wave spectra resembling turbulence. *Science*, *204*(4395), 832–835. https://doi.org/10.1126/science.204.4395.832

Dewan, E. M. (1994). The saturated-cascade model for atmospheric gravity wave spectra, and the wavelength-period (W-P) relations. *Geophysical Research Letters*, *21*(9), 817–820. https://doi.org/10.1029/94GL00702

Dewan, E. M. (1997). Saturated-cascade similitude theory of gravity wave spectra. *Journal of Geophysical Research*, *102*(D25), 29799–29817. https://doi.org/10.1029/97JD02151

Dörnbrack, A., Kaifler, B., Kaifler, N., Rapp, M., Wildmann, N., Garhammer, M., et al. (2020). Unusual appearance of mother-of-pearl clouds above El Calafate, Argentina. *Weather*, *75*(12), 378–388. https://doi.org/10.1002/wea.3863

Gao, X., & Meriwether, J. W. (1998). Mesoscale airborne in situ and lidar observations of variance and spatial structure in the troposphere and stratosphere regions. *Journal of Geophysical Research*, *103*(D6), 6391–6396. https://doi.org/10.1029/97JD03080

Gardner, C. S. (1994). Diffusive filtering theory of gravity wave spectra in the atmosphere. *Journal of Geophysical Research*, *99*(D10), 20601–20622. https://doi.org/10.1029/94JD00819

Gardner, C. S., Hostetler, C. A., & Franke, S. J. (1993). Gravity wave models for the horizontal wave number spectra of atmospheric velocity and density fluctuations. *Journal of Geophysical Research*, *98*(D1), 1035–1049. https://doi.org/10.1029/92JD02051

Geldenhuys, M., Kaifler, B., Preusse, P., Ungermann, J., Alexander, P., Krasauskas, L., et al. (2023). Observations of gravity wave refraction and its causes and consequences. *Journal of Geophysical Research: Atmospheres*, *128*(3), e2022JD036830. https://doi.org/10.1029/2022JD036830

Harvey, V. L., Randall, C. E., Bailey, S. M., Becker, E., Chau, J. L., Cullens, C. Y., et al. (2022). Improving ionospheric predictability requires accurate simulation of the mesospheric polar vortex. *Frontiers in Astronomy and Space Sciences*, *9*. https://doi.org/10.3389/fspas.2022.1041426

Hostetler, C. A., & Gardner, C. S. (1994). Observations of horizontal and vertical wave number spectra of gravity wave motions in the stratosphere and mesosphere over the mid-Pacific. *Journal of Geophysical Research*, *99*(D1), 1283–1302. https://doi.org/10.1029/93JD02927

Hostetler, C. A., Gardner, C. S., Vincent, R. A., & Lesicar, D. (1991). Spectra of gravity wave density and wind perturbations observed during ALOHA-90 on the 25 march flight between Maui and Christmas Island. *Geophysical Research Letters*, *18*(7), 1325–1328. https://doi.org/10.1029/91GL01150

Kaifler, B., Büdenbender, C., Mahnke, P., Damm, M., Sauder, D., Kaifler, N., & Rapp, M. (2017). Demonstration of an iron fluorescence lidar operating at 372 nm wavelength using a newly-developed Nd:YAG laser. *Optics Letters*, *42*(15), 2858–2861. https://doi.org/10.1364/OL.42.002858

Kaifler, B., & Kaifler, N. (2021). A compact Rayleigh autonomous lidar (CORAL) for the middle atmosphere. *Atmospheric Measurement Techniques*, *14*(2), 1715–1732. https://doi.org/10.5194/amt-14-1715-2021

Kim, Y.-J., Eckermann, S. E., & Chun, H.-Y. (2003). An overview of the past, present and future of gravity wave drag parametrization for numerical climate and weather prediction models. *Atmosphere-Ocean*, *41*(1), 65–98. https://doi.org/10.3137/ao.410105

Kogure, M., Yue, J., & Liu, H. (2021). Gravity wave weakening during the 2019 Antarctic stratospheric sudden warming. *Geophysical Research Letters*, *48*(8), e2021GL092537. https://doi.org/10.1029/2021GL092537

Kohma, M., Sato, K., Nishimura, K., & Tsutsumi, M. (2021). Weakening of polar mesosphere winter echo and turbulent energy dissipation rates after a stratospheric sudden warming in the Southern Hemisphere in 2019. *Geophysical Research Letters*, *48*(10), e2021GL092705. https://doi.org/10.1029/2021GL092705

Krasauskas, L., Kaifler, B., Rhode, S., Ungermann, J., Woiwode, W., & Preusse, P. (2023). Oblique propagation and refraction of gravity waves over the Andes observed by GLORIA and ALIMA during the SouthTRAC campaign. *Journal of Geophysical Research: Atmospheres*, *128*(10), e2022JD037798. https://doi.org/10.1029/2022JD037798

Kwon, K. H., Senft, D. C., & Gardner, C. S. (1990). Airborne sodium lidar observations of horizontal and vertical wave number spectra of mesopause density and wind perturbations. *Journal of Geophysical Research*, *95*(D9), 13723–13736. https://doi.org/10.1029/JD095iD09p13723

Li, Q., & Lindborg, E. (2018). Weakly or strongly nonlinear mesoscale dynamics close to the tropopause? *Journal of the Atmospheric Sciences*, *75*(4), 1215–1229. https://doi.org/10.1175/jas-d-17-0063.1

Lilly, D. K., & Petersen, E. L. (1983). Aircraft measurements of atmospheric kinetic energy spectra. *Tellus*, *35A*(5), 379–382. https://doi.org/10.1111/j.1600-0870.1983.tb00212.x

Lim, E.-P., Hendon, H. H., Butler, A. H., Thompson, D. W. J., Lawrence, Z. D., Scaife, A. A., et al. (2021). The 2019 Southern Hemisphere stratospheric polar vortex weakening and its impacts. *Bulletin of the American Meteorological Society*, *102*(6), E1150–E1171. https://doi.org/10.1175/bams-d-20-0112.1

Lindborg, E. (2006). The energy cascade in a strongly stratified fluid. *Journal of Fluid Mechanics*, *550*(-1), 207–242. https://doi.org/10.1017/S0022112005008128

Menchaca, M. Q., & Durran, D. R. (2019). The influence of gravity waves on the slope of the kinetic energy spectrum in simulations of idealized midlatitude cyclones. *Journal of the Atmospheric Sciences*, *76*(7), 2103–2122. https://doi.org/10.1175/JAS-D-18-0329.1

Nastrom, G. D., Fritts, D. C., & Gage, K. S. (1987). An investigation of terrain effects on the mesoscale spectrum of atmospheric motions. *Journal of the Atmospheric Sciences*, *44*(20), 3087–3096. https://doi.org/10.1175/1520-0469(1987)044<3087:aioteo>2.0.co;2

Nastrom, G. D., & Gage, K. S. (1985). A climatology of atmospheric wavenumber spectra of wind and temperature observed by commercial aircraft. *Journal of the Atmospheric Sciences*, *42*(9), 950–960. https://doi.org/10.1175/1520-0469(1985)042<0950:acoaws>2.0.co;2

Plougonven, R., de la Cámara, A., Hertzog, A., & Lott, F. (2020). How does knowledge of atmospheric gravity waves guide their parameterizations? *Quarterly Journal of the Royal Meteorological Society*, *146*(728), 1529–1543. https://doi.org/10.1002/qj.3732

Rapp, M., Kaifler, B., Dörnbrack, A., Gisinger, S., Mixa, T., Reichert, R., et al. (2021). SOUTHTRAC-GW: An airborne field campaign to explore gravity wave dynamics at the World's strongest hotspot. *Bulletin of the American Meteorological Society*, *102*(4), E871–E893. https://doi.org/10.1175/bams-d-20-0034.1

Rodriguez Imazio, P., Mininni, P. D., Godoy, A., Rivaben, N., & Dörnbrack, A. (2023). Not all clear air turbulence is Kolmogorov—The fine-scale nature of atmospheric turbulence. *Journal of Geophysical Research: Atmospheres*, *128*(2), e2022JD037491. https://doi.org/10.1029/2022JD037491

Selz, T., Bierdel, L., & Craig, G. C. (2019). Estimation of the variability of mesoscale energy spectra with three years of COSMO-DE analyses. *Journal of the Atmospheric Sciences*, *76*(2), 627–637. https://doi.org/10.1175/JAS-D-18-0155.1

Shen, X., Wang, L., & Osprey, S. (2020). Tropospheric forcing of the 2019 Antarctic sudden stratospheric warming. *Geophysical Research Letters*, *47*(20), e2020GL089343. https://doi.org/10.1029/2020GL089343

Sun, Y. Q., Rotunno, R., & Zhang, F. (2017). Contributions of moist convection and internal gravity waves to building the atmospheric -5/3 kinetic energy spectra. *Journal of the Atmospheric Sciences*, *74*(1), 185–201. https://doi.org/10.1175/jas-d-16-0097.1

VanZandt, T. E. (1982). A universal spectrum of buoyancy waves in the atmosphere. *Geophysical Research Letters*, *9*(5), 575–578. https://doi.org/10.1029/GL009i005p00575

Waite, M. L., & Snyder, C. (2009). The mesoscale kinetic energy spectrum of a baroclinic life cycle. *Journal of the Atmospheric Sciences*, *66*(4), 883–901. https://doi.org/10.1175/2008jas2829.1